

Efficient photocatalytic hydrogen peroxide generation coupled with selective benzylamine oxidation over defective ZrS_3 nanobelts

Zhangliu Tian^{1,2}, Cheng Han ^{1✉}, Yao Zhao^{2,3}, Wenrui Dai², Xu Lian ², Yanan Wang⁴, Yue Zheng⁴, Yi Shi ², Xuan Pan^{1,4}, Zhichao Huang^{1,4}, Hexing Li ⁵ & Wei Chen ^{2,3,4✉}

Photocatalytic hydrogen peroxide (H_2O_2) generation represents a promising approach for artificial photosynthesis. However, the sluggish half-reaction of water oxidation significantly limits the efficiency of H_2O_2 generation. Here, a benzylamine oxidation with more favorable thermodynamics is employed as the half-reaction to couple with H_2O_2 generation in water by using defective zirconium trisulfide (ZrS_3) nanobelts as a photocatalyst. The ZrS_3 nanobelts with disulfide (S_2^{2-}) and sulfide anion (S^{2-}) vacancies exhibit an excellent photocatalytic performance for H_2O_2 generation and simultaneous oxidation of benzylamine to benzonitrile with a high selectivity of >99%. More importantly, the S_2^{2-} and S^{2-} vacancies can be separately introduced into ZrS_3 nanobelts in a controlled manner. The S_2^{2-} vacancies are further revealed to facilitate the separation of photogenerated charge carriers. The S^{2-} vacancies can significantly improve the electron conduction, hole extraction, and kinetics of benzylamine oxidation. As a result, the use of defective ZrS_3 nanobelts yields a high production rate of 78.1 ± 1.5 and $32.0 \pm 1.2 \mu\text{mol h}^{-1}$ for H_2O_2 and benzonitrile, respectively, under a simulated sunlight irradiation.

¹SZU-NUS Collaborative Innovation Center for Optoelectronic Science & Technology, International Collaborative Laboratory of 2D Materials for Optoelectronics Science and Technology of Ministry of Education, Institute of Microscale Optoelectronics, Shenzhen University, Shenzhen, China.

²Department of Chemistry, National University of Singapore, 3 Science Drive 3, Singapore, Singapore. ³Joint School of National University of Singapore and Tianjin University, International Campus of Tianjin University, Binhai New City, Fuzhou, China. ⁴Department of Physics, National University of Singapore, 2 Science Drive 3, Singapore, Singapore. ⁵International Joint Lab on Resource Chemistry, College of Chemistry and Materials Science, Shanghai Normal University, Shanghai, China. ✉email: hancheng@szu.edu.cn; phycw@nus.edu.sg

Artificial photosynthesis, i. e. the conversion of solar energy into chemical energy, is considered as one of the promising approaches to synthesize chemicals with the unlimited energy source and minimized environmental problems^{1,2}. As a promising liquid solar fuel generated by artificial photosynthesis, hydrogen peroxide (H_2O_2) has attracted growing attention because of its high commercial value and low transportation cost³. Substantial efforts have been devoted to the development of effective photocatalysts or photocathodes for the H_2O_2 generation from water and O_2 ^{4–6}. In the photocatalytic process, the sluggish oxidation of water induced by the photogenerated valence holes is a limiting factor for the production of H_2O_2 ^{7–11}. Most previous reports focused on improving the half-reaction of O_2 reduction, e. g. by consuming holes with sacrificial agents, such as isopropyl alcohol, benzyl alcohol, and 2-PrOH^{3,12,13}. However, the development of an alternative oxidation reaction with accelerated kinetics to produce value-added chemicals was rarely reported. On the other hand, selective oxidation of amines to nitriles with lower oxidation potential than water plays an vital role in both laboratorial and industrial synthetic process since nitriles are the important intermediates during the synthesis of fine chemicals, pharmaceuticals, and agrochemicals^{14–21}. Intensive research has been carried out to synthesize nitriles from primary amines through dehydrogenation^{22–28}. However, most of the reactions are conducted in organic solvents under harsh conditions, such as high-temperature, exposure to high-pressure oxygen or air, and presence of oxidants. Photocatalytic reactions have been demonstrated to be an effective approach to synthesize nitriles under mild conditions^{29–31}, but previous works were seriously limited by the use of noble metals as the co-catalysts to realize the dehydrogenation in organic solvents. Thus, the development of artificial photosynthesis in an aqueous and easy scale-up condition with earth-abundant photocatalysts is highly desirable for the production of nitriles in an economically-viable and environment-friendly way.

Monoclinic zirconium trisulfide (ZrS_3) (ICCD PDF no. 30-1498), a layered n-type transition metal trichalcogenide (TMT), has recently drawn great research interest due to the extraordinary properties arising from its unique disulfide anions (S_2^{2-})³². ZrS_3 has shown a good optical responsivity of 290 mA W^{-1} with an in-plane hole and electron mobility at a magnitude of 10^2 and $10^3 \text{ cm}^2 \text{ V}^{-1} \text{ s}^{-1}$, respectively^{33–36}. In particular, ZrS_3 possesses a bandgap of $\sim 2 \text{ eV}$ with a more negative conduction band minimum (CBM) than the H_2 evolution potential³⁷, making ZrS_3 a promising semiconductor for photocatalytic and photoelectrochemical applications. The previous studies on zirconium nitride have demonstrated that its superior performance for O_2 reduction stems from the interaction between Zr sites and oxide species, where the Zr d-orbitals make a strong contribution³⁸. Intriguingly, the conduction band of ZrS_3 is mainly composed of Zr d-orbitals^{33,35}, which has a much more negative potential than the reducing potential of O_2 to H_2O_2 . Therefore, ZrS_3 shows great potential for the photocatalytic H_2O_2 generation.

There are three categories of S (S_1 , S_2 , and S_3) environments in monoclinic ZrS_3 lattice, where S_1 denotes the sulfide ion (S^{2-}) and S_2 , S_3 are interpreted as the S_2^{2-} (Fig. 1a, b)³⁹. Recently, both theoretical calculations and experimental investigations have demonstrated that moderate S_2^{2-} vacancies can greatly promote the separation of photogenerated charge carriers in TMTs (Supplementary Fig. 1a and b)^{40,41}. In addition, the anion vacancies existing on the surface of n-type semiconductors can further improve its photocatalytic and photoelectrochemical performance by accelerating the kinetics of hole transfer on the surface^{42–45}. The crystal structure analysis of ZrS_3 inspires us that the S_2^{2-} and S^{2-} vacancies can be separately introduced into ZrS_3 by different methods (Fig. 1 and Supplementary Fig. 1). Experimentally, hexagonal ZrS_2 (ICCD PDF no. 11-0679) is usually obtained by

vacuum annealing of monoclinic ZrS_3 at elevated temperatures. This suggests that ZrS_3 can desulfurize into ZrS_2 by the post-annealing at a higher temperature under vacuum⁴⁶. Only one type of Zr (Zr_1) and S (S_1) environment exists in ZrS_2 , where the Zr_1 - S_1 bond length is similar to that in ZrS_3 (Fig. 1a–c). Besides, ZrS_2 shows a similar layered structure to ZrS_3 , and atomic layers in both materials are parallel to the (001) plane (Supplementary Fig. 1c–f). When ZrS_3 transforms into ZrS_2 , it does not need much tweaking of the framework along both [010] and [001] directions (Supplementary Fig. 1c and e), but it is required to adjust the framework along the [100] direction (Fig. 1d and f). Figure 1 clearly suggests that the ZrS_3 can transform into ZrS_2 by two steps: the first step can be the desulfurization of ZrS_3 to release S_2 or S_3 ions to form a distorted crystal structure of ZrS_2 (Fig. 1a, b, d, and e), and then the distorted crystal structure undergoes structural relaxation by tuning the length and angle of Zr-S bonds to form ZrS_2 without breaking or regrouping the bonds (Fig. 1b, c, e, and f). Thus, the high-temperature vacuum annealing is expected to be an effective scheme to produce S_2^{2-} vacancies in ZrS_3 . On the other hand, S^{2-} ions have high adaptability when coordinated with metal ions, which can serve as either terminal or bridge ions to interact with metals (especially for alkali metals). This different from the S_x^{2-} ($x \geq 2$) ions that are difficult to bond with metals (Supplementary Fig. 1g)⁴⁷. Moreover, ZrS_3 is easily formed as nanobelts (NBs) with rich S^{2-} ions exposed at the edges (Supplementary Fig. 1h and i). Previous studies have used active metals such as Mg, Al, and Zn to induce oxygen vacancies in metal oxide due to their reducibility⁴⁸. Compared to these metals, alkali metal lithium (Li) has a higher reducibility and can be easily intercalated into host materials. Li can be easily dissolved in solvents like ammonia or ethanedi-amine to form Li-based complex for the solvothermal treatment, which has been widely utilized to enhance the transition temperature of superconducting materials^{49–51} and in particular to induce oxygen vacancies on TiO_2 ⁵². Therefore, such Li-based treatment could be an effective approach to induce S^{2-} vacancies on ZrS_3 .

Here, ZrS_3 NBs with both S_2^{2-} and S^{2-} vacancies are employed to enhance the photocatalytic production of H_2O_2 coupled with the selective oxidation of benzylamine to benzonitrile in water. The impacts of S_2^{2-} and S^{2-} vacancies on modulating the charge carrier dynamics and photocatalytic performance are systematically investigated. The S_2^{2-} vacancies can significantly facilitate the separation of photogenerated charge carriers; while the S^{2-} vacancies are demonstrated to not only promote the electron conduction and hole extraction in the photocatalytic process but also improve the kinetics of benzylamine oxidation. As a result, the use of defective ZrS_3 NBs as photocatalyst produces H_2O_2 and benzonitrile at a high rate of 78.1 ± 1.5 and $32.0 \pm 1.2 \mu\text{mol h}^{-1}$ respectively, under the illumination of a simulated sunlight.

Results and discussions

Structural properties and band structures of photocatalysts.

ZrS_3 NBs were synthesized via a chemical vapor transport of S powder to Zr powder using iodine as a transport agent. ZrS_3 with S_2^{2-} vacancies (ZrSS_{2-x}) was obtained by the re-annealing of the as-grown ZrS_3 NBs at $700 \text{ }^\circ\text{C}$ for different time (10, 15, and 20 min) under vacuum. ZrSS_{2-x} with S^{2-} vacancies ($\text{ZrS}_{1-y}\text{S}_{2-x}$) was prepared through a low-temperature solvothermal treatment by using Li-dissolved ethanedi-amine with different amounts of Li (50, 100, and 150 mg). We denote ZrSS_{2-x} NBs annealed for X time as $\text{ZrSS}_{2-x}(\text{X})$ and $\text{ZrS}_{1-y}\text{S}_{2-x}$ NBs annealed for X min and treated with Y mg Li as $\text{ZrS}_{1-y}\text{S}_{2-x}(\text{X}/\text{Y})$. The x-ray diffraction (XRD) pattern indicates the formation of ZrS_3 in the monoclinic phase (ICCD PDF no. 30-1498), and the vacuum annealing and

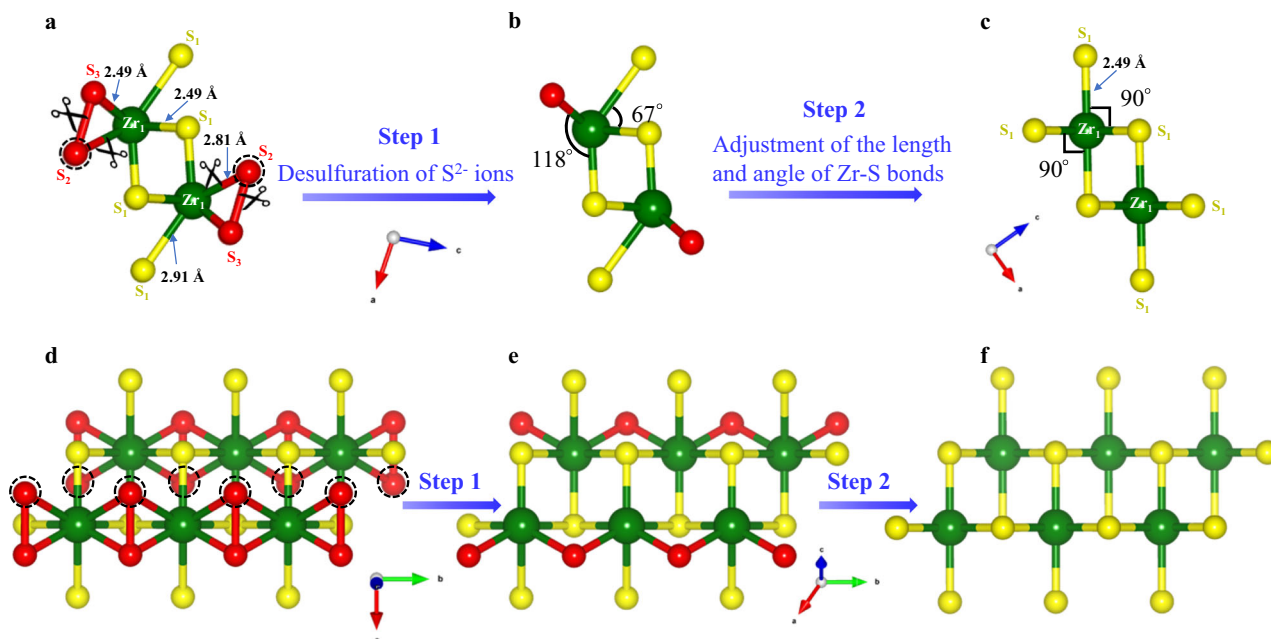


Fig. 1 The transformation of the crystal structure of ZrS_3 into ZrS_2 . The schematic process of the transformation of monoclinic ZrS_3 (ICCD PDF no. 30-1498) into hexagonal ZrS_2 (ICCD PDF no. 11-0679) from the [010] (**a–c**) and [001] (**d–f**) views. **a, d** Crystal structure of monolayer ZrS_3 with a boundary of $1 \times 3 \times 1$ from the [010] and [001] views, respectively. **b, e** Crystal structure of monolayer ZrS_3 after desulfuration of S_2^{2-} ions from **a** and **d**, respectively. **c, f** Crystal structure of monolayer ZrS_2 with a boundary of $1 \times 3 \times 1$ from the [010] and [001] views, respectively.

further Li treatment did not induce any phase transition in $\text{ZrSS}_{2-x}(15)$ and $\text{ZrS}_{1-y}\text{S}_{2-x}(15/100)$ NBs (Supplementary Fig. 2). However, the samples show decreased peak intensity from the ZrS_3 to the $\text{ZrS}_{1-y}\text{S}_{2-x}(15/100)$ NBs, due to the introduction of sulfur vacancies that reduce the crystallinity of ZrS_3 , as observed in the high-resolution transmission electron microscopy (HRTEM) image (Supplementary Fig. 3). The obtained ZrS_3 was formed as NBs with the width ranging from 300 nm to 3 μm and length in tens of micrometers (Fig. 2a–c). Scanning electron microscope (SEM) and atomic force microscope (AFM) measurements were further conducted to statistically determine the length, width, and thickness distribution of ZrS_3 NBs. The average length, width, and thickness of NBs were measured to be 24 μm , 840 nm, and 38 nm, respectively (Supplementary Figs. 4 and 5), where all the histograms exhibit a unimodal distribution with the peak in the range of 20–30 μm , 0.6–1.0 μm and 25–45 nm, respectively (Supplementary Fig. 4b, c and Supplementary Fig. 5d). As a result, the average ratio of width/thickness was calculated to be ~ 22 , which qualifies the label of “NBs” for our samples. The individual ZrS_3 NB is confirmed as the single crystal along [010] direction by the TEM and corresponding selected area electron diffraction (SAED) characterization (Fig. 2d). It is demonstrated that the ZrS_3 layer is parallel to the axial direction of NB, which is in favor of charge carrier transport⁴⁰. As shown in the HRTEM images (Supplementary Fig. 3), ZrS_3 exhibits highly-ordered lattice fringes with an excellent crystallinity, while $\text{ZrS}_{1-y}\text{S}_{2-x}(15/100)$ shows an obvious lattice disorder with relatively poor crystallinity. This suggests that the introduction of sulfur vacancies could lead to a decreased crystallinity in ZrS_3 , consistent with the XRD results.

As shown in the diffuse reflectance UV–vis spectra (Fig. 2e), both ZrS_3 and $\text{ZrSS}_{2-x}(15)$ NBs absorb light with the wavelength up to ~ 650 nm, corresponding to a bandgap of 2.02 eV (Supplementary Fig. 6). $\text{ZrS}_{1-y}\text{S}_{2-x}(15/100)$ NBs present a slight red-shift of absorption spectrum, revealing a smaller bandgap of 1.98 eV. The Mott–Schottky plots for all three samples exhibit positive slopes, indicating the n-type behavior of ZrS_3 (Fig. 2f).

These results were obtained by measuring the photocatalysts deposited on the fluorine-doped tin oxide (FTO) substrate. It is worth noting that the deposition process did not induce any obvious change of the photocatalyst (Supplementary Fig. 7a–c), suggesting that the sample on the FTO substrate measured with the photoelectrochemical set-up is essentially the same photocatalyst. The flat band potentials (E_{fb}) of ZrS_3 , $\text{ZrSS}_{2-x}(15)$, and $\text{ZrS}_{1-y}\text{S}_{2-x}(15/100)$ are estimated to be -0.10 , -0.11 , and -0.18 V versus reversible hydrogen electrode (V_{RHE}), respectively (Fig. 2g and Supplementary Fig. 7d). E_{fb} is commonly used to estimate the CBM for a series of n-type semiconductors at the surface in an aqueous environment, which agreed with their theoretically determined values^{1,44,53–55}. Previous studies on the energy positions of semiconductors have shown that the CBM of zirconium-based sulfides is very close to their E_{fb} ^{37,54}, and therefore the CBM of ZrS_3 , $\text{ZrSS}_{2-x}(15)$, and $\text{ZrS}_{1-y}\text{S}_{2-x}(15/100)$ can be directly determined by their E_{fb} . Based on the Mott–Schottky (Fig. 2f, g, and Supplementary Fig. 7d) and UV–vis spectra results, the CBM and valance band maximum (VBM) for ZrS_3 , $\text{ZrSS}_{2-x}(15)$, and $\text{ZrS}_{1-y}\text{S}_{2-x}(15/100)$ were revealed to be -0.10 , -0.11 , -0.18 V_{RHE} (CBM) and 1.92, 1.91, and 1.80 V_{RHE} (VBM), respectively (Fig. 2h and Supplementary Fig. 8). The CBMs of ZrS_3 , $\text{ZrSS}_{2-x}(15)$, and $\text{ZrS}_{1-y}\text{S}_{2-x}(15/100)$ are higher than the potential for two-electron reduction of O_2 . Previous studies have shown that the oxidation potential of benzylamine lies higher than that of water, and the benzylamine oxidation was thus used to replace oxygen evolution reaction to couple with photocatalytic and electrocatalytic hydrogen evolution reaction^{14,17,55,56}. This suggests the VBM of defective ZrS_3 NBs lying far below the oxidation potential of benzylamine, indicating that these photocatalysts are applicable to the photocatalytic O_2 reduction and benzylamine oxidation.

Characterizations of vacancy structure. Four characteristic Raman modes of ZrS_3 located at ~ 147 , 274, 315, and 524 cm^{-1} were observed in Fig. 3a, which are assigned to the rigid chain vibration (I: A_g^{rigid}), internal out-of-plane vibrations

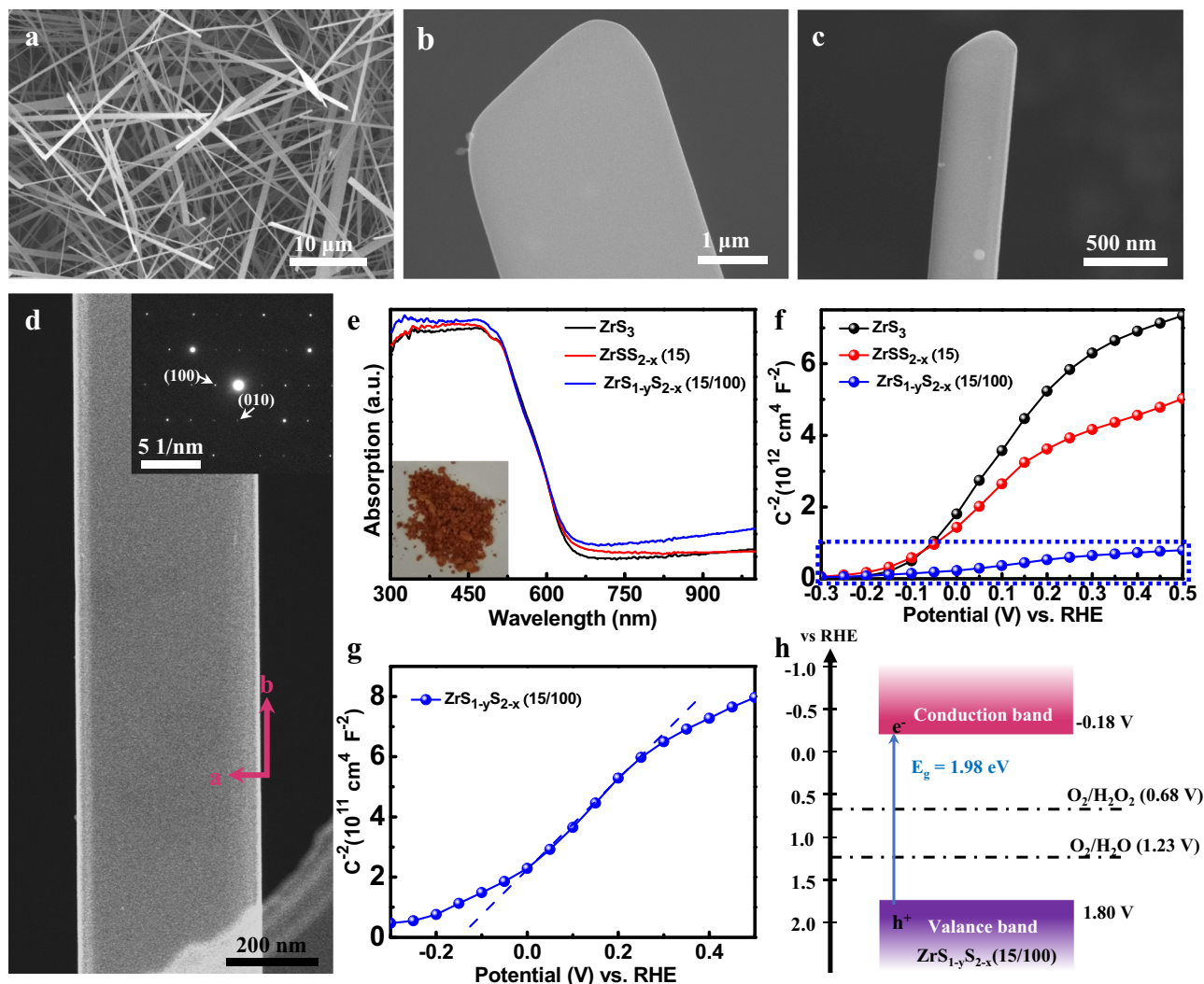


Fig. 2 Structural properties and band structures of defective ZrS_3 NBs. **a** Top-sectional, **b**, **c** high-magnification SEM images of the ZrS_3 NBs. **d** TEM image and SAED pattern of single ZrS_3 NB. **e** Diffuse reflectance UV-vis spectra of the ZrS_3 , $\text{ZrSS}_{2-x}(15)$ and $\text{ZrS}_{1-y}\text{S}_{2-x}(15/100)$ NBs. Inset, the photograph of the $\text{ZrS}_{1-y}\text{S}_{2-x}(15/100)$ NBs. **f** Mott-Schottky plots of ZrS_3 , $\text{ZrSS}_{2-x}(15)$ and $\text{ZrS}_{1-y}\text{S}_{2-x}(15/100)$ NBs and **g** Mott-Schottky plot of $\text{ZrS}_{1-y}\text{S}_{2-x}(15/100)$ magnified from **f**. **h** Schematic band structure diagram for $\text{ZrS}_{1-y}\text{S}_{2-x}(15/100)$. To have a clear view of the single NB, the sample for this SEM measurement was prepared by evaporating the isopropanol dispersion of ZrS_3 NBs.

(II: A_g^{internal} and III: A_g^{internal}), and S-S diatomic motion (IV: $A_g^{\text{s-s}}$), respectively³⁵. The Raman spectra show an obvious red-shift of $A_g^{\text{s-s}}$ mode by $\sim 5 \text{ cm}^{-1}$ from ZrS_3 , $\text{ZrSS}_{2-x}(15)$, and $\text{ZrS}_{1-y}\text{S}_{2-x}(15/100)$, originating from the introduction of S_2^{2-} vacancies⁴⁰. We also observed a $\sim 3 \text{ cm}^{-1}$ red-shift of A_g^{rigid} mode from ZrS_3 and $\text{ZrSS}_{2-x}(15)$ to $\text{ZrS}_{1-y}\text{S}_{2-x}(15/100)$. Since the A_g^{rigid} is correlated to the vibration of quasi-one-dimensional chains in the direction of *c* axis (Supplementary Fig. 9a), the shift of A_g^{rigid} mode in $\text{ZrS}_{1-y}\text{S}_{2-x}(15/100)$ results from the introduction of S_2^{2-} vacancies, which alters the length of Zr-S bonds within each chain. The similar shift of A_g^{rigid} mode was also identified from ZrS_3 and $\text{ZrSS}_{2-x}(15)$ to the only Li-treated ZrS_3 with 100 mg Li ($\text{ZrS}_{1-y}\text{S}(100)$) as shown in Supplementary Fig. 9b. To explore the effect of process parameters during the synthesis of defective materials on the types and density of defects, and the correlation with photocatalytic activity, orthogonal experiments have been performed by simultaneously changing the Li amount and vacuum annealing duration. All the samples were further examined by the Raman characterization, and Supplementary Fig. 10a–d show representative Raman spectra of the defective ZrS_3 NBs separately

treated by the Li-treatment with different Li amount and by the vacuum annealing for different time. The gradual red-shift of A_g^{rigid} mode (difference from 1.6 to 6.1 cm^{-1}) was observed with increasing Li amount, resulting from the increased concentration of S_2^{2-} vacancies in Li-treated ZrS_3 NBs (Supplementary Fig. 10a and b). Similarly, the vacuum annealing triggered a red-shift of $A_g^{\text{s-s}}$ mode due to the generated S_2^{2-} vacancies⁴⁰, which was enlarged from 2.4 to 8.1 cm^{-1} by prolonging the annealing time (Supplementary Fig. 10c and d). Based on the Raman results, the shifts of both A_g^{rigid} and $A_g^{\text{s-s}}$ modes for all the samples were extracted and plotted as 3D histograms, as shown in Supplementary Figure 11a and b. The A_g^{rigid} shift only depends on the Li amount, while the $A_g^{\text{s-s}}$ shift only relies on the annealing time. These results reveal that the S_2^{2-} and S^{2-} vacancies in $\text{ZrS}_{1-y}\text{S}_{2-x}$ can be independently induced by the vacuum annealing and Li-treatment respectively, and the concentration of vacancies can be further controlled by varying the annealing time and Li amount.

The XPS characterization was conducted on these samples to further confirm the vacancy type. After the vacuum annealing, the $\text{ZrSS}_{2-x}(15)$ NBs exhibit a slightly lower binding energy of the

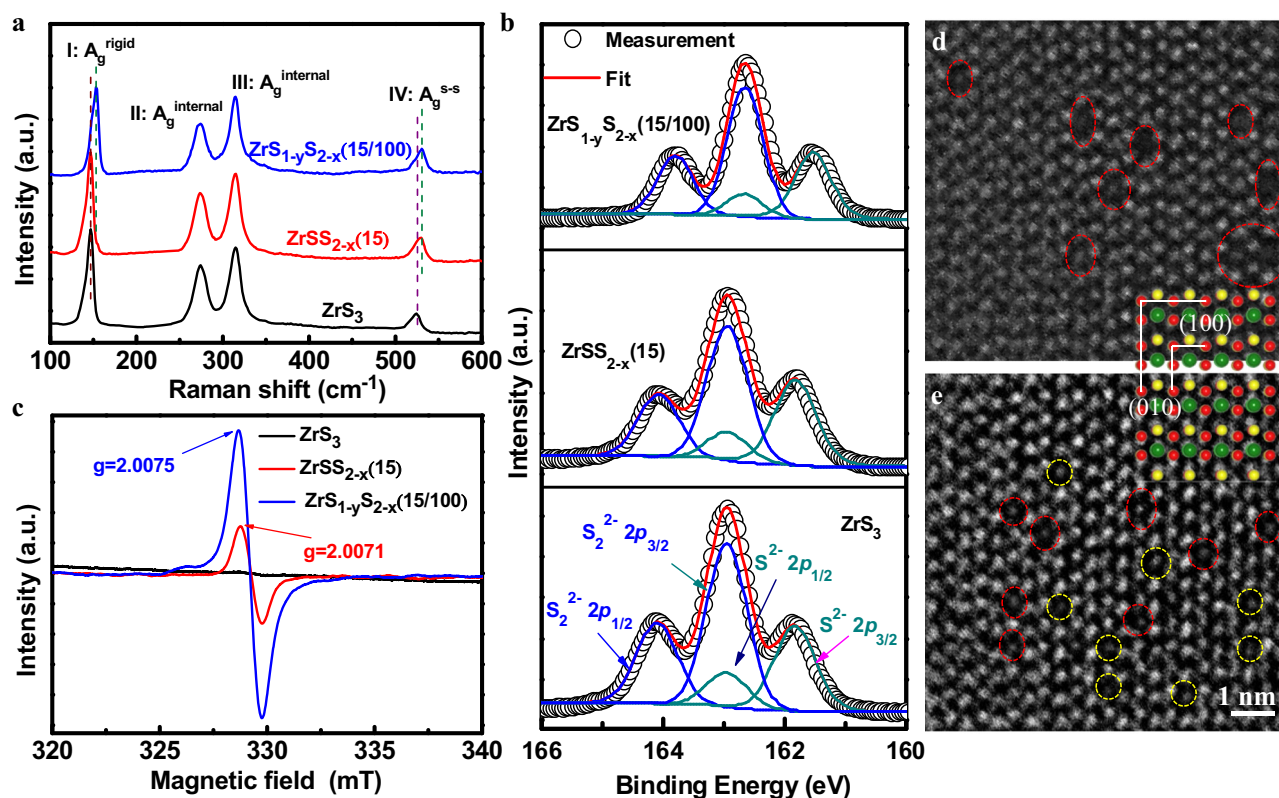


Fig. 3 Characterizations of vacancy structure of defective ZrS_3 NBs. **a** Raman spectra, **b** S 2p XPS spectra, and **c** EPR spectra of the ZrS_3 , $\text{ZrSS}_{2-x}(15)$ and $\text{ZrS}_{1-y}\text{S}_{2-x}(15/100)$ NBs. HAADF-STEM images of **d** $\text{ZrSS}_{2-x}(15)$ and **e** $\text{ZrS}_{1-y}\text{S}_{2-x}(15/100)$ measured from a spherical aberration-corrected TEM. Inset: the crystal lattice of ZrS_3 along the [001] orientation. The red and yellow circles represent S_2^{2-} and S^{2-} , respectively.

Zr 3d core level than ZrS_3 NBs, consistent with the results from ZrS_3 to ZrS_2 (Supplementary Fig. 12a)⁵⁷. Furthermore, $\text{ZrSS}_{2-x}(15)$ shows a significant attenuation of $\text{S}_2^{2-} 2p$ peaks with the nearly unchanged $\text{S}^{2-} 2p$ peaks compared to ZrS_3 (Fig. 3b and Supplementary Fig. 12b), indicating the mere increase of S_2^{2-} vacancies in $\text{ZrSS}_{2-x}(15)$. It is worth noting that no clear peak shift was observed for $\text{ZrSS}_{2-x}(15)$, which results from the almost retained electron density around the S sites, as revealed by the Mott-Schottky results. After further Li treatment, both Zr 3d and S 2p core levels of $\text{ZrS}_{1-y}\text{S}_{2-x}(15/100)$ NBs shifted to the lower binding energy by ~ 0.3 eV regarding $\text{ZrSS}_{2-x}(15)$ (Supplementary Fig. 12a, c, and d), due to the increased electron density around the S sites induced by S^{2-} vacancies⁵⁸. In particular, the intensity of $\text{S}^{2-} 2p$ peaks in the $\text{ZrS}_{1-y}\text{S}_{2-x}(15/100)$ was clearly lower than that of $\text{ZrSS}_{2-x}(15)$ (Fig. 3b and Supplementary Fig. 12d), revealing the increase of S^{2-} vacancies. This phenomenon has been commonly observed in the transition metal sulfide with S^{2-} vacancies such as MoS_2 , In_2S_3 , and CuInS_2 ^{59–61}. The similar variation of Zr 3d and S 2p spectra observed from ZrS_3 to $\text{ZrS}_{1-y}\text{S}_{2-x}(100)$ further suggest the separate introduction of S^{2-} vacancies by the Li treatment (Supplementary Fig. 12a and c). The type and density of sulfur vacancies for all the samples were further quantitatively analyzed by the XPS characterization, and representative S 2p XPS spectra of the defective ZrS_3 NBs separately treated by the vacuum annealing and Li-treatment are presented in Supplementary Fig. 13a and b, respectively. The x and y values in the label of $\text{ZrS}_{1-y}\text{S}_{2-x}$ for all the samples were estimated from the XPS results by calculating the area ratio of characteristic peaks in defective samples to that of ZrS_3 , as summarized in Supplementary Table 1. Agreed with the Raman results, the vacuum annealing and Li-treatment can independently attenuate the intensity of $\text{S}_2^{2-} 2p$ and $\text{S}^{2-} 2p$ peaks,

respectively, as revealed by the almost unchanged x and y values under the identical annealing time and Li amount, respectively. For an intuitive comparison, the x and y values as a function of the annealing time and Li amount were plotted in 3D histograms, as shown in Supplementary Fig. 14a and b, respectively. The x was estimated to be 0.20 ± 0.01 , 0.36 ± 0.01 , and 0.49 ± 0.01 for the annealing time of 10, 15, and 20 min, respectively; while the y was evaluated to be 0.05 ± 0.01 , 0.36 ± 0.01 , and 0.49 ± 0.01 for 50, 100, and 150 mg Li, respectively.

In addition, the electron paramagnetic resonances (EPR) investigation was also carried out to detect the vacancy structure. A characteristic peak can be clearly detected at $g = 2.0071$ for all the vacuum annealed samples in Supplementary Fig. 15a, and the peak intensity is proportional to the vacuum annealing duration. This suggested the characteristic peak of Zr- S_2^{2-} dangling bonds is located at $g = 2.0071$ ⁵⁸. Similarly, the characteristic peak of Zr- S^{2-} dangling bonds is located at $g = 2.0082$ (Supplementary Fig. 15b). Therefore, the characteristic peak located at $g = 2.0075$ for $\text{ZrS}_{1-y}\text{S}_{2-x}(15/100)$ NBs suggests the formation of both S^{2-} and S_2^{2-} vacancies (Fig. 3c). The higher signal intensity of $\text{ZrS}_{1-y}\text{S}_{2-x}(15/100)$ than that of $\text{ZrSS}_{2-x}(15)$ indicates more sulfur vacancies existing in $\text{ZrS}_{1-y}\text{S}_{2-x}(15/100)$ NBs⁶⁰. To have a direct view of the atomic arrangement for $\text{ZrSS}_{2-x}(15)$ and $\text{ZrS}_{1-y}\text{S}_{2-x}(15/100)$ NBs, the high-angle annular dark-field scanning transmission electron microscopy (HAADF-STEM) images were obtained, where the atomic sites can be determined by comparing the HAADF-STEM image with the crystal structure of ZrS_3 lattice along the [001] direction (Supplementary Fig. 15c and d). The $\text{ZrSS}_{2-x}(15)$ demonstrates the missing atoms only emerging on the S_2^{2-} sites, as indicated by the red dashed circles in Fig. 3d, while the atomic vacancies exist on both S^{2-} (indicated by yellow dashed circles) and S_2^{2-} sites for $\text{ZrS}_{1-y}\text{S}_{2-x}(15/100)$ (Fig. 3e).

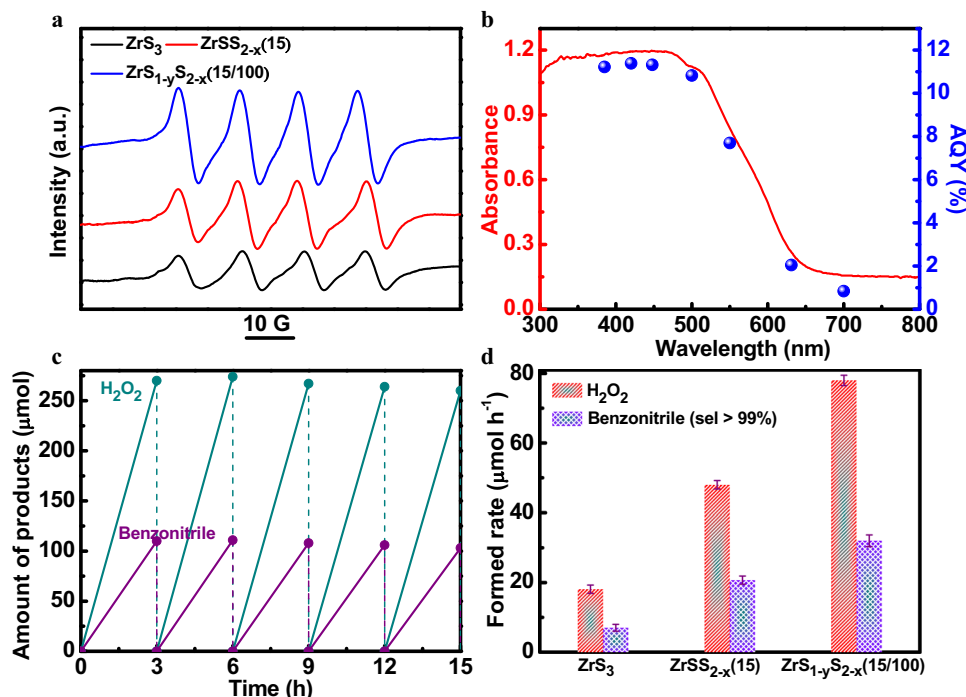


Fig. 4 The photocatalytic properties of defective ZrS_3 NBs. **a** EPR spectra of ZrS_3 , $\text{ZrSS}_{2-x}(15)$ and $\text{ZrS}_{1-y}\text{S}_{2-x}(15/100)$ in the presence of DMPO. **b** Absorption spectrum of $\text{ZrS}_{1-y}\text{S}_{2-x}(15/100)$ and its dependence of AQY with monochromatic light irradiation. Conditions: 30 ml aqueous solution with 1 mmol benzyl alcohol, 50 mg photocatalysts. **c** Results of H_2O_2 and benzonitrile generation for a repeated photoreaction sequence with $\text{ZrS}_{1-y}\text{S}_{2-x}(15/100)$ under AM1.5G simulated sunlight irradiation. **d** H_2O_2 and benzonitrile evolution rate by the respective photocatalysts under AM1.5G simulated sunlight irradiation. Error bars are the standard error of the mean for 9 independent samples. Conditions: 30 ml H_2O with 1 mmol benzylamine, 50 mg photocatalysts, 1 bar O_2 .

Photocatalytic performance. The photocatalytic capability of the defective ZrS_3 NBs for reducing O_2 to create the reactive oxygen species (ROS) was first evaluated by the EPR trapping experiment using 5,5-dimethyl-1-pyrroline N-oxide (DMPO). As illustrated in Fig. 4a, four characteristic peaks of $\text{DMPO-O}_2^{\bullet-}$ were observed for all NBs, confirming the generation of $\text{O}_2^{\bullet-}$ ^{60,62,63}. The introduction of S_2^{2-} vacancies was found to enhance the reduction of O_2 to $\text{O}_2^{\bullet-}$, and the additional introduction of S^{2-} vacancies led to a further increased photocatalytic activity. The correlation of types and density of sulfur vacancies with photocatalytic activity was further examined by the iodometry¹² under the irradiation of AM1.5G simulated sunlight with the presence of benzyl alcohol as the hole scavenger. As shown in Supplementary Figure 16, the $\text{ZrS}_{1-y}\text{S}_{2-x}(15/100)$ NBs with the $x = 0.36$ and $y = 0.13$ (16.3% sulfur vacancies) exhibit the best performance for photocatalytic H_2O_2 generation. When the Li amount and annealing time were simultaneously less than 150 mg and 20 min, respectively, the photocatalytic activity increased with the increase of both S_2^{2-} and S^{2-} vacancies. When the Li amount reached 150 mg or the annealing time reached 20 min, the photocatalytic activity showed an increase at the early stage and then decreased with the increase of annealing time or Li amount, respectively. This indicates that it is harmful to further improve photocatalytic activity with excessive either S_2^{2-} or S^{2-} vacancies. This is because excessive sulfur vacancies could act as the recombination centers for photogenerated charge carriers for photogenerated charge carriers. To determine the H_2O_2 formed rate, the production was analyzed by iodometry (Supplementary Fig. 17)¹². The $\text{ZrS}_{1-y}\text{S}_{2-x}(15/100)$ NBs possess a high H_2O_2 evolution rate of $89.6 \pm 1.5 \mu\text{mol h}^{-1}$ with good reproducibility (Supplementary Fig. 18) in the presence of benzyl alcohol as the hole scavenger (entry 5 in Supplementary Table 2), which is higher than most previous reports (Supplementary Table 3). The

wavelength-dependent apparent quantum yield (AQY) for the H_2O_2 generation on $\text{ZrS}_{1-y}\text{S}_{2-x}(15/100)$ agrees well with its absorption spectrum, revealing that the photocatalytic activity originates from the bandgap excitation of $\text{ZrS}_{1-y}\text{S}_{2-x}(15/100)$ (Fig. 4b). In particular, $\text{ZrS}_{1-y}\text{S}_{2-x}(15/100)$ produces an AQY of 11.4 and 10.8% for the incident light of 400 and 500 nm respectively and demonstrates a good activity even with the excitation extended to the near-infrared region of ~ 700 nm. Furthermore, the photocatalyst of $\text{ZrS}_{1-y}\text{S}_{2-x}(15/100)$ is able to maintain its activity after being recycled for the same reaction with both presence of benzylamine and benzyl alcohol, as presented in Fig. 4c and Supplementary Fig. 19a. After the stability measurement, no noticeable change was observed in the XRD patterns and Raman spectra, revealing good structure stability (Supplementary Fig. 19b and c). In addition, the $\text{S } 2p$ XPS spectra of $\text{ZrS}_{1-y}\text{S}_{2-x}(15/100)$ after the repeated photoreaction show a weak peak located at ~ 168.7 eV (Supplementary Fig. 19d), suggesting a slight surface oxidation of $\text{ZrS}_{1-y}\text{S}_{2-x}(15/100)$ after the photocatalytic measurement.

Based on the high activity of $\text{ZrS}_{1-y}\text{S}_{2-x}(15/100)$ for H_2O_2 generation, we further utilized benzylamine to substitute the hole scavenger. The H_2O_2 evolution rate of $\text{ZrS}_{1-y}\text{S}_{2-x}(15/100)$ was decreased to $78.1 \pm 1.5 \mu\text{mol h}^{-1}$ with the same molar amount of benzylamine as benzyl alcohol, due to the slower oxidation kinetics of benzylamine than that of benzyl alcohol. Simultaneously, the benzylamine was oxidized and converted to benzonitrile at a rate of $32.0 \pm 1.2 \mu\text{mol h}^{-1}$ with a high selectivity of $>99\%$ (entry 2 in Supplementary Table 2 and Fig. 4d), and no other by-products were detected by the Gas Chromatography-Mass Spectrometry measurements (Supplementary Fig. 20), consistent with the previous report^{14,29}. Besides, the $\text{ZrS}_{1-y}\text{S}_{2-x}(15/100)$ photocatalyst shows the rates for decomposition of H_2O_2 of 0.14 and 0.16 h^{-1} with the presence of benzyl

alcohol and benzylamine, respectively, and the rates for formation of H_2O_2 of 125 and 113 $\mu\text{mol h}^{-1}$ with the presence of benzyl alcohol and benzylamine, respectively (Supplementary Fig. 17b). Similar photocatalytic behaviors were also identified on both $\text{ZrSS}_{2-x}(15)$ and ZrS_3 NBs, which produced the H_2O_2 at a rate of 58.5 ± 1.7 and $30.3 \pm 1.3 \mu\text{mol h}^{-1}$ with the hole scavenger (entry 3 and 1 in Supplementary Table 2), respectively. As a comparison, $\text{ZrSS}_{2-x}(15)$ and ZrS_3 show a decreased H_2O_2 evolution rate of 48.0 ± 1.2 and $18.1 \pm 1.2 \mu\text{mol h}^{-1}$ with the use of benzylamine, and the corresponding benzonitrile generation rates are 20.7 ± 1.2 and $7.0 \pm 1.0 \mu\text{mol h}^{-1}$, respectively (Fig. 4d). As a result, the comparison of photocatalytic performance among $\text{ZrS}_{1-y}\text{S}_{2-x}(15/100)$, $\text{ZrSS}_{2-x}(15)$, and ZrS_3 reveals the key role of S_2^{2-} and S^{2-} vacancies on the O_2 reduction and benzylamine oxidation.

To provide a deep insight into the effect of defective structures in ZrS_3 NBs on its photocatalytic performance, the transient open-circuit potential measurements were performed on ZrS_3 , $\text{ZrSS}_{2-x}(15)$, and $\text{ZrS}_{1-y}\text{S}_{2-x}(15/100)$ NBs to reveal the lifetime of photo-induced charge carriers (Supplementary Fig. 21 and Supplementary Equation 4)⁶⁴. After introducing S_2^{2-} vacancies, the carrier lifetime of $\text{ZrSS}_{2-x}(15)$ was significantly increased to 0.69 s as compared to 0.3 s of ZrS_3 , while the $\text{ZrS}_{1-y}\text{S}_{2-x}(15/100)$ exhibits a further enhanced lifetime of 0.82 s, as shown in Fig. 5a. The increased photocurrent for the defective ZrS_3 also suggests the role of S_2^{2-} and S^{2-} vacancies on improving the carrier lifetime and dynamics (Supplementary Fig. 22). In order to explore the underlying mechanism for the lifetime enhancement, the charge carrier dynamics of these samples were extracted through the Mott–Schottky method. According to the Mott–Schottky equation (Supplementary Equation 1), the electron concentrations of ZrS_3 , $\text{ZrSS}_{2-x}(15)$, and $\text{ZrS}_{1-y}\text{S}_{2-x}(15/100)$ NBs were calculated to be 4.00×10^{18} , 5.35×10^{18} , and $4.58 \times 10^{19} \text{ cm}^{-3}$, based on the estimated width of the depletion region (w_d) under the illumination of 55, 46, and 17 nm, respectively (Supplementary

Equation 2). The similar band bending between ZrS_3 and $\text{ZrSS}_{2-x}(15)$ suggests that the significantly enhanced carrier lifetime in $\text{ZrSS}_{2-x}(15)$ is attributed to the role of S_2^{2-} vacancies in reducing electron-hole recombination rather than band bending, in agreement with the previous theoretical calculation⁴¹. The significantly reduced w_d in $\text{ZrS}_{1-y}\text{S}_{2-x}(15/100)$ indicates a large electric field strength on the surface of $\text{ZrS}_{1-y}\text{S}_{2-x}(15/100)$, which can accelerate the extraction of photogenerated holes towards the surface and limit the internal band-to-band recombination. Moreover, the small w_d in $\text{ZrS}_{1-y}\text{S}_{2-x}(15/100)$ results in a large conduction region for the free electrons compared to ZrS_3 and $\text{ZrSS}_{2-x}(15)$, which is beneficial for the electron transport.

On the other hand, the reaction kinetics of benzylamine oxidation on the photocatalysts were also investigated by the intensity-modulated photocurrent spectroscopy (IMPS). The typical IMPS plots and the generalized reaction schematics are shown in Supplementary Fig. 23, and the details for the calculation of rate constant of charge transfer (k_t) and surface recombination (k_{rec}) are discussed in the supporting information. Since the $k_t/(k_t + k_{\text{rec}})$ can evaluate the efficiency of charge carrier transfer between the catalyst and reactant⁴³, the clearly higher $k_t/(k_t + k_{\text{rec}})$ of $\text{ZrS}_{1-y}\text{S}_{2-x}(15/100)$ than those of $\text{ZrSS}_{2-x}(15)$ and ZrS_3 indicates that $\text{ZrS}_{1-y}\text{S}_{2-x}(15/100)$ possesses higher efficiency for benzylamine oxidation (Fig. 5b). Furthermore, $\text{ZrSS}_{2-x}(15)$ presents a slightly higher $k_t/(k_t + k_{\text{rec}})$ compared to ZrS_3 , as derived from their similar behaviors of k_t and k_{rec} (Fig. 5c and d). The similar k_{rec} between $\text{ZrSS}_{2-x}(15)$ and ZrS_3 is mainly ascribed to their similar surface band bending extracted from the Mott–Schottky results (Supplementary Fig. 7d). $\text{ZrS}_{1-y}\text{S}_{2-x}(15/100)$ with the larger surface band bending thus shows a significantly decreased k_{rec} . The slightly decreased k_{rec} of $\text{ZrSS}_{2-x}(15)$ compared to ZrS_3 originates from the suppression of surface charge recombination by S_2^{2-} vacancies. The similar behavior of k_t for $\text{ZrSS}_{2-x}(15)$ and ZrS_3 indicates that the introduction of S_2^{2-}

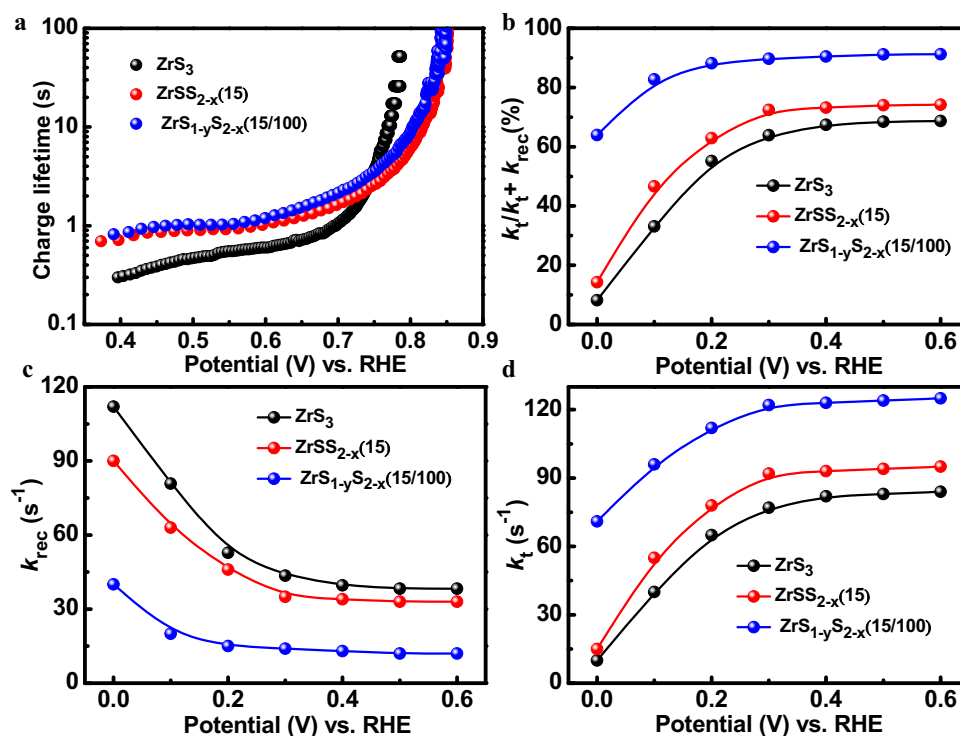


Fig. 5 The charge carrier dynamics of the photocatalysts. **a** The charge carrier lifetime of ZrS_3 , $\text{ZrSS}_{2-x}(15)$, and $\text{ZrS}_{1-y}\text{S}_{2-x}(15/100)$ NBs. **b** Ratio of $k_t/(k_t + k_{\text{rec}})$, rate constants **c** k_t and **d** k_{rec} of ZrS_3 , $\text{ZrSS}_{2-x}(15)$, and $\text{ZrS}_{1-y}\text{S}_{2-x}(15/100)$ for benzylamine oxidation measured in 0.5 M Na_2SO_4 with 0.1 M benzylamine.

vacancies have a subtle effect on its catalytic capability for benzylamine oxidation. Furthermore, the large increase of k_t for $ZrS_{1-y}S_{2-x}(15/100)$ compared to $ZrSS_{2-x}(15)$ and ZrS_3 suggests that the S^{2-} vacancies can act as an additional photocatalytic layer for the benzylamine oxidation (Fig. 5d).

In summary, we have developed an efficient photocatalyst of $ZrS_{1-y}S_{2-x}(15/100)$ NBs with S^{2-} and S^- vacancies for the integration of photocatalytic H_2O_2 generation with the selective oxidation of benzylamine to benzonitrile in water. More importantly, the unique S^{2-} vacancies and S^- vacancies can be controllably induced in the defective ZrS_3 NBs by varying the annealing time and Li amount, which promise a prospective strategy for defect engineering. With the introduction of S^{2-} vacancies, the charge carrier recombination is prominently suppressed, and the surface S^{2-} vacancies are revealed to improve the electron conduction, surface hole extraction, and kinetics of benzylamine oxidation. As a result, the photocatalyst of $ZrS_{1-y}S_{2-x}(15/100)$ exhibits a high generation rate of 78.1 ± 1.5 and $32.0 \pm 1.2 \mu\text{mol h}^{-1}$ for H_2O_2 and benzonitrile, respectively. Furthermore, $ZrS_{1-y}S_{2-x}(15/100)$ NBs possesses a photoexcitation up to ~ 700 nm and delivers a high AQY of 11.4 and 10.8% under the incident light of 400 and 500 nm, respectively.

Methods

Preparation of ZrS_3 , $ZrSS_{2-x}$, and $ZrS_{1-y}S_{2-x}$ NBs. The ZrS_3 NBs were synthesized through a typical chemical vapor transport process. 0.96 g S (99.5% purity, Alfa Aesar) and 0.91 g Zr (99.2% purity, Sigma-Aldrich) powders were mixed, and 5 mg iodine (99.5% purity, Alfa Aesar) was added as a transport agent. The mixture was sealed in a quartz ampoule (Φ 6 mm \times 200 mm) under the vacuum of 10^{-3} Pa, which was subsequently placed in the center of a two-zone furnace with a temperature gradient of ca. 15 K/cm from center to edge. The furnace was heated to 650 °C and last for 10 h to produce ZrS_3 powder, which has a pure monoclinic crystal structure that is stable at this temperature. The obtained 1.87 g ZrS_3 powder was then dispersed in isopropanol ($\geq 99.5\%$ purity, Alfa Aesar) at a concentration of 0.5 mg ml^{-1} followed by the sonication for 15 min. The dispersion was subsequently centrifuged for 10 min at 1006 xg to remove large aggregates. Finally, about 0.6 g ZrS_3 NBs (32% yield) were obtained by the collection from the rest of the dispersion by further centrifugation for 10 min at 16099 xg.

Since hexagonal ZrS_2 (ICCD PDF no. 11-0679) is usually obtained by vacuum annealing of monoclinic ZrS_3 at elevated temperature (820 °C)⁴⁶. This suggests that ZrS_3 can be desulfurized into ZrS_2 by the post-annealing at a higher temperature under vacuum. It is implied that such transformation can also be realized by the desulfuration of S^{2-} ions, based on our previous results on TiS_3 and crystal structure analysis between ZrS_2 and ZrS_3 in Fig. 1 and Supplementary Fig. 1⁴⁰. As a result, the $ZrSS_{2-x}$ NBs were prepared using the previously reported vacuum annealing method. Specifically, 0.6 g ZrS_3 NBs were sealed in the quartz ampoule (Φ 6 mm \times 10 mm) again, which was then heated to 700 °C and last for different time (10, 15, and 20 mins) to fabricate $ZrSS_{2-x}$ NBs. Besides, a certain amount of Li metal pieces (50, 100, and 150 mg) were added into 30 ml ethanediamine ($\geq 98\%$ purity, Sigma-Aldrich) for continuous magnetic stirring in an Ar-filled glovebox ($O_2, H_2O < 0.1$ ppm). After the Li was completely dissolved, 0.5 g $ZrSS_{2-x}$ NBs were added into the solution, and the obtained solution was subsequently transferred into a 50 mL Teflon-lined autoclave and sealed immediately. Then, the Teflon-lined autoclave was taken out of the glovebox and kept in an oven at 120 °C for 24 h. After cooling down to room temperature, the mixture was first washed in 0.2 M HCl and then rinsed several times in deionized water and ethanol, where the $ZrS_{1-y}S_{2-x}$ NBs (yield > 96%) was finally obtained.

Characterization of photocatalysts. UV-Vis-NIR spectrometer (Hitachi U4100), field emission SEM (FE-SEM, JEOL JSM6700F), TEM (FEI Titan 80-300, operated at 200 kV), XRD (Bruker D8 Advance), XPS (ESCALAB 250Xi) with Al K α X-ray as the excitation source, EPR (JEOL FA200), tapping-mode AFM (MPF-3D, Asylum Research, CA, USA), and Raman spectroscopy (Horiba Jobin Yvon Modular Raman Spectrometer) with 514 nm laser excitation were employed to characterize different properties of the defective ZrS_3 NBs, e.g. atomic and energy band structure. In particular, the samples for the TEM measurements were suspended in ethanol and supported onto a holey carbon film on a Cu grid.

Coupling photocatalytic H_2O_2 generation with selective benzylamine oxidation over ZrS_3 , $ZrSS_{2-x}$, $ZrS_{1-y}S_{2-x}$ NBs. 50 mg photocatalyst was dispersed in 30 ml H_2O with 1 mmol benzylamine. After the sonication for a few seconds, the

mixed solution was bubbled by oxygen for 30 s. Subsequently, the solution was sealed and irradiated under an AM 1.5G simulated sunlight of 100 mW cm^{-2} derived from a 300 W xenon lamp fitted with an AM 1.5 filter. At certain time intervals, the solution was filtrated by a 0.22 μm Millipore filter to remove the photocatalyst. The aqueous and organic phase products were then analyzed by the iodometry and gas chromatograph (GC) measurements, respectively.

The production of H_2O_2 was analyzed by the iodometry¹². Typically, 50 μL 0.4 M potassium iodide (KI, $\geq 99\%$ purity, Sigma-Aldrich) aqueous solution and 50 μL 0.1 M potassium hydrogen phthalate ($\geq 99.5\%$ purity, Sigma-Aldrich) aqueous solution were added to 2ml obtained aqueous phase product, which was kept for 0.5 h. The mixed solution was then detected by UV-vis spectroscopy on the basis of absorbance at 350 nm, from which the quantity of generated H_2O_2 was estimated. In addition, to analyze organic phase product from the benzylamine oxidation, the organic liquid was first extracted using ethyl acetate ($\geq 99.9\%$ purity, Sigma-Aldrich) and then detected by the GC characterization. Fih

Photocatalytic H_2O_2 generation with benzyl alcohol as hole sacrificial reagent.

50 mg catalyst was dispersed in 30 ml H_2O containing 1mmol benzyl alcohol. After sonicating for a few seconds, the mixed solution was bubbled by oxygen for few seconds. Subsequently, the solution was sealed and irradiated under an AM 1.5G simulated sunlight of 100 mW cm^{-2} derived from a 300 W xenon lamp fitted with an AM 1.5 filter. The amount of H_2O_2 was analyzed by the iodometry. For the action spectrum analysis, the reactions were performed at 298 K under monochromated light irradiation, with the Φ_{AQY} (AQY, apparent quantum yield) determined by the following Eq. (1):

$$\Phi_{AQY}(\%) = \frac{[H_2O_2 \text{ formed (mol)}] \times 2}{[\text{photon number entered into the reactor (mol)}]} \times 100 \quad (1)$$

The stability test for $ZrS_{1-y}S_{2-x}(15/100)$ NBs. The $ZrS_{1-y}S_{2-x}(15/100)$ NBs was recovered by centrifugation for 15 min at 16,099g and used for the reaction sequence, with water replaced every 3 h during photoirradiation.

EPR trapping measurements. 4 mg catalyst was suspended in 500 μL CH_3OH containing 50 μL DMPO (Sigma-Aldrich for ESR-spectroscopy). After the sonication, the solution was irradiated by a 300 W xenon lamp with a 420 nm filter for 3 min. The resulted solution was subjected to the analysis by using a JEOL (FA200) ESR Spectrometer.

Photoelectrochemical measurements. The photoelectrochemical measurements were performed in a three-electrode system with an electrochemical workstation (Zahner Zennium) under an AM 1.5G simulated sunlight of 100 mW cm^{-2} (150 W, Newport 94011A LCS-100). The samples on FTO substrates were firstly prepared by a typical electrophoretic deposition method. For details, 25 ml acetone solution containing 20 mg sample and 40 mg iodine was used as the electrophoresis solution. The experimental setup consists of two pieces of FTO that serve as the anodic and cathodic electrodes, respectively. The FTO substrates were immersed in the above solution in parallel with a distance of 1cm, which were kept in the solution for 5 min at a 10 V bias under the potentiostat control. After being calcined for 2 h in a vacuum oven at 100 °C, a uniform film was firmly coated on the FTO substrates. Samples on FTO substrates were directly used as the working electrode, with a Pt wire and an Ag/AgCl (KCl saturated) electrode as counter and reference electrodes respectively. All the samples were illuminated through the sample side (front-side illumination). The photoelectrochemical performance was recorded in 0.1 M Na_2SO_4 electrolyte with 0.1 mM benzylamine. Mott-Schottky plots were derived from impedance-potential tests conducted at a frequency of 1 kHz in dark. IMPS spectra were recorded by the Zahner Zennium C-IMPS system.

Data availability

All data supporting the findings in the article as well as the Supplementary Information files are available from the corresponding authors on reasonable request.

Received: 8 September 2020; Accepted: 3 March 2021;

Published online: 01 April 2021

References

- Shiraishi, Y. et al. Resorcinol-formaldehyde resins as metal-free semiconductor photocatalysts for solar-to-hydrogen peroxide energy conversion. *Nat. Mater.* **18**, 985–993 (2019).
- Chen, S., Takata, T. & Domen, K. Particulate photocatalysts for overall water splitting. *Nat. Rev. Mater.* **2**, 1–17 (2017).
- Kofuji, Y. et al. Hydrogen peroxide production on a carbon nitride-boron nitride-reduced graphene oxide hybrid photocatalyst under visible light. *ChemCatChem* **10**, 2070–2077 (2018).

- Hou, H., Zeng, X. & Zhang, X. Production of hydrogen peroxide by photocatalytic processes. *Angew. Chem. Int. Ed.* **59**, 2–23 (2020).
- Fan, W. et al. Efficient hydrogen peroxide synthesis by metal-free polyterthiophene via photoelectrocatalytic dioxygen reduction. *Energy Environ. Sci.* **13**, 238–245 (2020).
- Hennessey, S. & Farras, P. Production of solar chemicals: gaining selectivity with hybrid molecule/semiconductor assemblies. *Chem. Commun.* **54**, 6662–6680 (2018).
- Teranishi, M., Naya, S.-i & Tada, H. In situ liquid phase synthesis of hydrogen peroxide from molecular oxygen using gold nanoparticle-loaded titanium (IV) dioxide photocatalyst. *J. Am. Chem. Soc.* **132**, 7850–7851 (2010).
- Kato, S., Jung, J., Suenobu, T. & Fukuzumi, S. Production of hydrogen peroxide as a sustainable solar fuel from water and dioxygen. *Energy Environ. Sci.* **6**, 3756–3764 (2013).
- Moon, G.-h, Kim, W., Bokare, A. D., Sung, N.-e & Choi, W. Solar production of H₂O₂ on reduced graphene oxide–TiO₂ hybrid photocatalysts consisting of earth-abundant elements only. *Energy Environ. Sci.* **7**, 4023–4028 (2014).
- Isaka, Y., Oyama, K., Yamada, Y., Suenobu, T. & Fukuzumi, S. Photocatalytic production of hydrogen peroxide from water and dioxygen using cyano-bridged polynuclear transition metal complexes as water oxidation catalysts. *Catal. Sci. Technol.* **6**, 681–684 (2016).
- Kim, H.-i, Kwon, O. S., Kim, S., Choi, W. & Kim, J.-H. Harnessing low energy photons (635 nm) for the production of H₂O₂ using upconversion nanohybrid photocatalysts. *Energy Environ. Sci.* **9**, 1063–1073 (2016).
- Wei, Z. et al. Efficient visible-light-driven selective oxygen reduction to hydrogen peroxide by oxygen-enriched graphitic carbon nitride polymers. *Energy Environ. Sci.* **11**, 2581–2589 (2018).
- Shiraishi, Y. et al. Selective hydrogen peroxide formation by titanium dioxide photocatalysis with benzylic alcohols and molecular oxygen in water. *ACS Catal.* **3**, 2222–2227 (2013).
- Huang, Y., Chong, X., Liu, C., Liang, Y. & Zhang, B. Boosting hydrogen production by anodic oxidation of primary amines over a NiSe nanorod electrode. *Angew. Chem. Int. Ed.* **57**, 13163–13166 (2018).
- Martin, A. & Kalevaru, V. N. Heterogeneously catalyzed ammoxidation: a valuable tool for one-step synthesis of nitriles. *ChemCatChem* **2**, 1504–1522 (2010).
- Jagadeesh, R. V., Junge, H. & Beller, M. Green synthesis of nitriles using non-noble metal oxides-based nanocatalysts. *Nat. Commun.* **5**, 1–8 (2014).
- Łuczak, T. Electrochemical behaviour of benzylamine, 2-phenylethylamine and 4-hydroxyphenylethylamine at gold. A comparative study. *J. Appl. Electrochem.* **38**, 43–50 (2007).
- Fleming, F. F., Yao, L., Ravikumar, P., Funk, L. & Shook, B. C. Nitrile-containing pharmaceuticals: efficacious roles of the nitrile pharmacophore. *J. Med. Chem.* **53**, 7902–7917 (2010).
- Wang, T. & Jiao, N. Direct approaches to nitriles via highly efficient nitrogenation strategy through C–H or C–C bond cleavage. *Acc. Chem. Res.* **47**, 1137–1145 (2014).
- Yan, G., Zhang, Y. & Wang, J. Recent advances in the synthesis of aryl nitrile compounds. *Adv. Synth. Catal.* **359**, 4068–4105 (2017).
- Liu, R. Y., Bae, M. & Buchwald, S. L. Mechanistic insight facilitates discovery of a mild and efficient copper-catalyzed dehydration of primary amides to nitriles using hydrosilanes. *J. Am. Chem. Soc.* **140**, 1627–1631 (2018).
- Feldhues, U. Oxidation of primary aliphatic amines to nitriles at the nickel hydroxide electrode. *Synthesis* **2**, 145–146 (1982).
- Semmelhack, M. F. & Schmid, C. R. Nitroxyl-mediated electro-oxidation of amines to nitriles and carbonyl compounds. *J. Am. Chem. Soc.* **105**, 6732–6734 (1983).
- Shono, T., Matsumura, Y. & Inoue, K. Electroorganic chemistry. 87. Indirect electrooxidation of amines to nitriles using halogen ions as mediators. *J. Am. Chem. Soc.* **106**, 6075–6076 (1984).
- Tseng, K.-N. T., Rizzi, A. M. & Szymczak, N. K. Oxidant-free conversion of primary amines to nitriles. *J. Am. Chem. Soc.* **135**, 16352–16355 (2013).
- Lambert, K. M. et al. Metal-free oxidation of primary amines to nitriles through coupled catalytic cycles. *Chem. Eur. J.* **22**, 5156–5159 (2016).
- Lambert, K. M. et al. Catalytic, metal-free oxidation of primary amines to nitriles. *Org. Synth.* **95**, 60–79 (2018).
- Dutta, I. et al. Double dehydrogenation of primary amines to nitriles by a ruthenium complex featuring pyrazole functionality. *J. Am. Chem. Soc.* **140**, 8662–8666 (2018).
- Ovoshchnikov, D. S., Donoeva, B. G. & Golovko, V. B. Visible-light-driven aerobic oxidation of amines to nitriles over hydrous ruthenium oxide supported on TiO₂. *ACS Catal.* **5**, 34–38 (2015).
- Tao, C. et al. Merging visible-light photoredox and copper catalysis in catalytic aerobic oxidation of amines to nitriles. *Org. Biomol. Chem.* **15**, 328–332 (2017).
- Zhu, P. et al. Photocatalytic selective aerobic oxidation of amines to nitriles over Ru/γ-Al₂O₃: the role of the support surface and the strong imine intermediate adsorption. *Catal. Sci. Technol.* **10**, 440–449 (2020).
- Wu, K. et al. Unusual lattice vibration characteristics in whiskers of the pseudo-one-dimensional titanium trisulfide TiS₃. *Nat. Commun.* **7**, 12952 (2016).
- Ahamed, R. et al. ZrS₃/MS₂ and ZrS₃/MX₂ (M Mo, W; X, Y S, Se, Te; X ≠ Y) type-II van der Waals hetero-bilayers: Prospective candidates in 2D excitonic solar cells. *Appl. Surf. Sci.* **499**, 143894 (2020).
- Yi, H. et al. The electronic band structure of quasi-one-dimensional van der Waals semiconductors: the effective hole mass of ZrS₃ compared to TiS₃. *J. Phys. Condens. Matter* **32**, 29LT01 (2020).
- Wang, X. et al. Highly polarized photoelectrical response in vdW ZrS₃ nanoribbons. *Adv. Electron. Mater.* **5**, 1900419 (2019).
- Tao, Y. R., Wu, X. C. & Xiong, W. W. Flexible visible-light photodetectors with broad photoresponse based on ZrS₃ nanobelt films. *Small* **10**, 4905–4911 (2014).
- Flores, E., Ares, J. R., Ferrer, I. J. & Sánchez, C. Synthesis and characterization of a family of layered trichalcogenides for assisted hydrogen photogeneration. *Phys. Status Solidi Rapid Res. Lett.* **10**, 802–806 (2016).
- Yuan, Y. et al. Zirconium nitride catalysts surpass platinum for oxygen reduction. *Nat. Mater.* **19**, 282–286 (2020).
- Endo, K., Ihara, H., Watanabe, K. & Gonda, S. I. XPS Study of one-dimensional compounds - TiS₃. *J. Solid State Chem.* **44**, 268–272 (1982).
- Tian, Z. et al. Enhanced charge carrier lifetime of TiS₃ photoanode by introduction of S₂²⁻ vacancies for efficient photoelectrochemical hydrogen evolution. *Adv. Funct. Mater.* **30**, 2001286 (2020).
- Wei, Y. Q., Zhou, Z. H. & Long, R. Defects slow down nonradiative electron-hole recombination in TiS₃ nanoribbons: a time-domain Ab initio study. *J. Phys. Chem. Lett.* **8**, 4522–4529 (2017).
- Tian, Z. et al. Hydrogen plasma reduced black TiO₂/B nanowires for enhanced photoelectrochemical water-splitting. *J. Power Sources* **325**, 697–705 (2016).
- Tian, Z. et al. Highly conductive cable-like bicomponent titania photoanode approaching limitation of electron and hole collection. *Adv. Funct. Mater.* **28**, 1803328 (2018).
- Tian, Z. et al. Novel black BiVO₄/TiO_{2-x} photoanode with enhanced photon absorption and charge separation for efficient and stable solar water splitting. *Adv. Energy Mater.* **9**, 1901287 (2019).
- Zhang, K. et al. Overcoming charge collection limitation at solid/liquid interface by a controllable crystal deficient overlayer. *Adv. Energy Mater.* **7**, 1600923 (2017).
- Li, L. et al. Electrical transport and high-performance photoconductivity in individual ZrS₂ nanobelts. *Adv. Mater.* **22**, 4151–4156 (2010).
- Kanatzidis, M. & Sutorik, A. (Karlin, K. D., Ed, 1995).
- Xu, J., Tian, Z., Yin, G., Lin, T. & Huang, F. Controllable reduced black titania with enhanced photoelectrochemical water splitting performance. *Dalton Trans.* **46**, 1047- (2017).
- Burrard-Lucas, M. et al. Enhancement of the superconducting transition temperature of FeSe by intercalation of a molecular spacer layer. *Nat. Mater.* **12**, 15–19 (2013).
- Hatake, T., Noji, T., Kawamata, T., Kato, M. & Koike, Y. New Li-ethylenediamine-intercalated superconductor Li_x(C₂H₈N₂)_yFe_{2-z}Se₂ with T_c = 45 K. *J. Phys. Soc. Jpn.* **82**, 123705 (2013).
- Scheidt, E.-W. et al. Superconductivity at T_c = 44 K in Li_xFe₂Se₂(NH₃)_y. *Eur. Phys. J. E Soft Matter* **85**, 1–5 (2012).
- Yin, G. et al. Hydrogenated blue titania for efficient solar to chemical conversions: preparation, characterization, and reaction mechanism of CO₂ reduction. *ACS Catal.* **8**, 1009–1017 (2018).
- Resasco, J. et al. TiO₂/BiVO₄ nanowire heterostructure photoanodes based on type II band alignment. *ACS Cent. Sci.* **2**, 80–88 (2016).
- Xu, Y. & Schoonen, M. A. The absolute energy positions of conduction and valence bands of selected semiconducting minerals. *Am. Mineral.* **85**, 543–556 (2000).
- Wang, Q. et al. Oxysulfide photocatalyst for visible-light-driven overall water splitting. *Nat. Mater.* **18**, 827–832 (2019).
- Liu, H., Xu, C., Li, D. & Jiang, H. L. Photocatalytic hydrogen production coupled with selective benzylamine oxidation over MOF composites. *Angew. Chem. Int. Ed. Engl.* **57**, 5379–5383 (2018).
- Jellinek, F., Pollak, R. & Shafer, M. X-ray photoelectron spectra and electronic structure of zirconium trisulfide and triselenide. *Mater. Res. Bull.* **9**, 845–856 (1974).
- Wang, X. et al. Single-atom vacancy defect to trigger high-efficiency hydrogen evolution of MoS₂. *J. Am. Chem. Soc.* **142**, 4298–4308 (2020).
- Li, H. et al. Corrigendum: activating and optimizing MoS₂ basal planes for hydrogen evolution through the formation of strained sulphur vacancies. *Nat. Mater.* **15**, 48–53 (2016).
- Sun, X. et al. Enhanced superoxide generation on defective surfaces for selective photooxidation. *J. Am. Chem. Soc.* **141**, 3797–3801 (2019).
- Li, X. et al. Selective visible-light-driven photocatalytic CO₂ reduction to CH₄ mediated by atomically thin CuIn₅S₈ layers. *Nat. Energy* **4**, 690–699 (2019).

62. Song, H., Wei, L., Chen, C., Wen, C. & Han, F. Photocatalytic production of H₂O₂ and its in situ utilization over atomic-scale Au modified MoS₂ nanosheets. *J. Catal.* **376**, 198–208 (2019).
63. Lei, J. et al. Robust photocatalytic H₂O₂ production over inverse opal g-C₃N₄ with carbon vacancy under visible light. *ACS Sustain. Chem. Eng.* **7**, 16467–16473 (2019).
64. Credgington, D. & Durrant, J. R. Insights from transient optoelectronic analyses on the open-circuit voltage of organic solar cells. *J. Phys. Chem. Lett.* **3**, 1465–1478 (2012).

Acknowledgements

The authors acknowledge the financial support from Singapore National Research Foundation under the grant of NRF2017NRF-NSFC001-007, NUS Flagship Green Energy Programme, Fundamental Research Foundation of Shenzhen (No. JCYJ20190808152607389 and No. JCYJ20170817100405375), China Postdoctoral Science Foundation (2020M672794), and Shenzhen Peacock Plan (No. KQTD2016053112042971).

Author contributions

T.Z., H.C., L.H. and C.W. conceived and designed the experiments. T.Z., Z.Y., D.W., L.X., W.Y. and Z.Y. performed the experiments. T.Z., L.X. and H.Z. analyzed the data. T.Z., S.Y., and P.X. wrote the manuscript. All authors discussed the results and commented on the manuscript.

Competing interests

The authors declare no competing interests.

Additional information

Supplementary information The online version contains supplementary material available at <https://doi.org/10.1038/s41467-021-22394-8>.

Correspondence and requests for materials should be addressed to C.H. or W.C.

Peer review information *Nature Communications* thanks Pau Farràs, Vladimir B. Golovko, and Lei Han for their contributions to the peer review of this work. Peer review reports are available.

Reprints and permission information is available at <http://www.nature.com/reprints>

Publisher's note Springer Nature remains neutral with regard to jurisdictional claims in published maps and institutional affiliations.



Open Access This article is licensed under a Creative Commons Attribution 4.0 International License, which permits use, sharing, adaptation, distribution and reproduction in any medium or format, as long as you give appropriate credit to the original author(s) and the source, provide a link to the Creative Commons license, and indicate if changes were made. The images or other third party material in this article are included in the article's Creative Commons license, unless indicated otherwise in a credit line to the material. If material is not included in the article's Creative Commons license and your intended use is not permitted by statutory regulation or exceeds the permitted use, you will need to obtain permission directly from the copyright holder. To view a copy of this license, visit <http://creativecommons.org/licenses/by/4.0/>.

© The Author(s) 2021